Multi-technical analysis of damage process in GFRP-bar reinforced concrete beam

Engineering Structures 348 (2026) 121803

Contents lists available at ScienceDirect

Engineering Structures

journal homepage: www.elsevier.com/locate/engstruct

Multi-technical analysis of damage process in GFRP-bar reinforced concrete beam

Zihan Jiang [a,b], Zhiwen Zhu [a,*], Leandro F. Friedrich [c], Ediblu S. Cezar [b], Jueliang Chen [d], Giuseppe Lacidogna [b,d,**], Ignacio Iturrioz [e]

[a] Department of Civil Engineering and Smart Cities, Shantou University, University Road 243, Shantou 515063, China
[b] Department of Structural, Geotechnical and Building Engineering, Politecnico di Torino, Corso Duca degli Abruzzi 24, Torino 10129, Italy
[c] Department of Mechanical Engineering, Universidade Federal do Pampa, Av. Tiaraju 810, CEP 97546-550 Alegrete, Brazil
[d] College of Architecture and Energy Engineering, Wenzhou University of Technology, Wenzhou 325000, China
[e] Mechanical Post-Graduate Program, Universidade Federal do Rio Grande do Sul, Sarmento Leite 425, CEP 90050-170 Porto Alegre, Brazil

ARTICLE INFO

Keywords:
Glass Fibre Reinforced Polymer
Acoustic Emission
Digital Image Correlation
Failure Precursor
Method of Critical Fluctuations
AE Entropy
Natural Time Analysis

ABSTRACT

Glass fibre-reinforced polymer (GFRP)-reinforced concrete can be defined as a next-generation structural material in which the reinforcing secondary phase consists in corrosion-resistant GFRP bars. This study investigates the damage process of GFRP-bar reinforced concrete beams through the acoustic emission (AE) and digital image correlation (DIC) techniques. Precursors to identify impending failure in GFRP-bar reinforced concrete beam are investigated by analysing the AE time series. This study verifies the efficiency of the so-called Method of Critical Fluctuations based (MCF-B) approach, alongside the Debski-Pradhan-Hansen (DPH) index, AE Entropy and Natural Time Analysis, as a failure precursor. The results show that: AE features can indicate the stick-slip behaviour between the GFRP bars and the concrete matrix, as evidenced by the tensile-to-shear crack transition obtained by the Rise Angle to Average Frequency (*RA-AF*) analysis; The MCF-B method effectively identifies the critical region, and its results align with the observations from Natural Time Analysis and AE Entropy Analysis; While *b*-value exhibits divergent trends beyond this critical region, MCF-B maintains its critical signature, demonstrating the method's robustness; Low entropy indicates a more ordered state in the system, suggesting that the structure is prepared for impending failure; In the experimental tests, the evolution of the DPH index is also calculated, and this parameter can be used to collect complementary information about the AE test.

1. Introduction

In recent years, the use of glass fibre-reinforced polymer (GFRP) bars as an equivalent reinforcement material to steel bars in concrete structures has been increasingly prevalent [1–4]. GFRP bars differ significantly from steel bars, primarily due to their much lower modulus of elasticity and structural anisotropy. In addition, GFRP bars have the characteristics of good non-magnetic properties, high tensile strength, good fatigue resistance and high corrosion resistance [5–8].

The good performance of GFRP-reinforced concrete relies on sufficient interfacial bonding between the bars and the concrete, which is a crucial parameter governing a behaviour of reinforced concrete members and transferring of the internal forces from concrete to the reinforcement [9–11]. The bond mechanism is governed by the mechanical interaction, chemical adhesion, and frictional forces between the GFRP rebar and the concrete [12]. In addition, it depends on the nominal diameter of the rebars, surface enhancement, concrete cover, bond length, and concrete strength [13].

In recent years, there has been increased interest in the complex dynamics of fracture phenomena, which involve multiple interacting entities that exhibit nonlinear behaviour and influence each other [14]. In the deformation of brittle materials, processes like grain dynamics,

* Corresponding author.
** Corresponding author at: Department of Structural, Geotechnical and Building Engineering, Politecnico di Torino, Corso Duca degli Abruzzi 24, Torino 10129, Italy
E-mail addresses: 19zhjiang@stu.edu.cn (Z. Jiang), zhuzw@stu.edu.cn (Z. Zhu), leandrofriedrich@unipampa.edu.br (L.F. Friedrich), ediblu.silvacezar@polito.it (E.S. Cezar), 20230011@wzut.edu.cn (J. Chen), giuseppe.lacidogna@polito.it (G. Lacidogna), ignacio@mecanica.ufrgs.br (I. Iturrioz).

https://doi.org/10.1016/j.engstruct.2025.121803
Received 19 August 2025; Received in revised form 11 October 2025; Accepted 14 November 2025
Available online 17 November 2025

micro-crack formation, and matrix heterogeneity lead to structural failure. Consequently, understanding these dynamics is crucial for various fields, from engineering design and maintenance to earthquake research [15–17].

Recent studies have focused on analysing time-series data from acoustic emission (AE) laboratory tests [18,19], aiming to improve precursor parameters indicating impending structural failures. In Refs. [20–22], AE signal amplitudes were found to follow the Gutenberg-Richter (GR) power law [23] commonly used in seismology. The *b*-value parameter was also examined to assess damage evolution in heterogeneous materials [24–27]. Previous researchers [28,29] have utilised this method to examine earthquake activity patterns by analysing temporal, spatial, and magnitude parameters. Nevertheless, investigations into long-range correlations in AE time series are still scarce [30]. Natural Time Analysis, originally proposed by Varotsos et al. [31] for Seismic Electrical Signals (SES), has shown promise in examining the dynamic evolution of complex systems, including earthquakes [32,33] and material fractures [34,35]. Among the approaches mentioned, the *b*-value method is the most relevant for analysing both earthquake and AE data [36,37]. A key issue when using the *b*-value is fitting the frequency-magnitude relationship according to the GR power law. Deviations from a linear relationship can arise from factors such as a lack of high-magnitude events and incomplete detection of low-magnitude events. Such deviations can undermine the reliability and accuracy of the *b*-value, which is essential for identifying failure precursors [38]. In terms of the data fitting process, Han et al. [38] analysed several methods for estimating the *b*-value from magnitude-frequency distributions, including their proposed Robust Fitting Method (RFM). In contrast, Birck et al. [39] offered an alternative explanation for the loss of linearity, suggesting it results from combining various damage mechanisms into a single analysis. On the other hand, some researchers have explored the loss of linearity in the frequency-magnitude relationship across various complex systems [40].

This paper investigated the damage process of GFRP-bar reinforced concrete beams through AE and digital image correlation (DIC) techniques. In addition, *RA-AF* analysis was used to analyse the crack pattern for the failure mode. In terms of time series analysis for identifying impending failure, four main approaches are examined: DPH index, Natural Time Analysis, AE Entropy Analysis and a novel Method of Critical Fluctuations (MCF-B). MCF is recognised for identifying criticality in seismic data [41,42]. The MCF-B method employs a function similar to MCF, incorporating two exponents (one potential and one exponential) to take into account deviations from linearity in the frequency-magnitude distribution of AE events. For all the methods, the behaviour of the parameters and their relationship with the criticality of the structure are analysed.

While each of these methods provides a unique perspective on damage evolution, their integrated application in this study is novel. This multi-technique framework is designed not as a simple parallel comparison, but to achieve cross-validation and a synergistic understanding of the critical failure state in GFRP-bar reinforced concrete.

2. Material and methods

2.1. Experimental program

In this sub-section the mechanical characterisation of the sample material is presented, followed by the description of the specimens and the adopted test procedures.

2.1.1. Material characterisation

The concrete mix was designed with reference to the Chinese standard JGJ 55–2019 [43]. The mix proportions by mass for the C100 grade concrete were as follows: cement 1.0, silica fume 0.20, fly ash 0.05, river sand 1.15, coarse aggregate 1.85, water 0.18, and a polycarboxylate superplasticizer 0.035. The concrete was cured under standard conditions for 28 days. This low water-cement ratio was enabled by the use of high-range water-reducing admixtures to ensure sufficient workability for casting, and it was selected to produce a C100 high-strength concrete suitable for investigating bond behaviour under high stress levels, which can occur in specialized structural applications.

To characterise the mechanical properties of the C100 concrete, cylindrical samples with a diameter of 150 mm and height of 300 mm, along with cubic samples with a side length of 150 mm, were cast together with the beam to determine the concrete strength, on the same day as the beam test. The compressive strength and splitting tensile strength were determined from the cubic concrete samples according to the Chinese standard GB/T 50081–2019 [44], while the elastic modulus was determined from the cylindrical samples. Table 1 lists the measured mechanical properties of the concrete, determined from samples tested on the same day as the beam. The exact average cubic compressive strength was 110.4 MPa, and the elastic modulus was 44.8 GPa.

The GFRP bars used in this experimental campaign were supplied by AOO SCIENCE Co., Ltd. As illustrated in Fig. 1, the bars featured a sand-coated surface with periodically spaced ribs to enhance bond performance with the concrete matrix. The specific type employed was a round bar with a nominal diameter of 12 mm and a center-to-center rib spacing of 10 mm, as shown in Table 2. GFRP bars are manufactured by impregnating alkali-free glass fibre pultrusion roving with various types of resin glue solution containing curing agents, promoters, and other additives. Under the traction of a pultrusion machine, the impregnated fibers pass through a preforming die and enter a heated steel die. Within this die, the resin system is cured at a controlled temperature range of 120°C to 140°C and under the consolidation pressure inherent to the pultrusion process, forming the final ribbed profile.

The mechanical properties of the GFRP bars, including the ultimate tensile strength and elastic modulus, were determined through direct tensile tests. The typical stress-strain behaviour was linear elastic up to failure, as shown in Fig. 1(d). The tensile tests of the GFRP bars were performed according to the Chinese standard GB/T 30022–2013 [45]. The average characteristic values are summarized in Table 2. A total of five specimens were tested. The average ultimate tensile strength was 1164 MPa with a standard deviation of 18.7 MPa and a coefficient of variation of 1.61 %. The average elastic modulus was 56.4 GPa, and the average failure strain was 2.07 %.

2.1.2. Experimental setup

Fig. 2 provides the details of the GFRP bar-reinforced concrete beams. The aim of the tests was to determine the bond behaviour of GFRP bars to concrete on the beam-bond setup. A total of three specimens were tested. The reinforcement ratio of 0.28 %, combined with the high-strength concrete, was designed to promote a bond-slip failure mode, isolating the bar-concrete interface behaviour for study. The mechanical behaviour and fracture patterns of three beams were tested, and one of the beams was selected for AE analysis. The concrete beam has a cross-sectional area of 200 × 200 mm and a total length of 1800 mm. The specimen, composed of two prismatic blocks, is connected by a GFRP bar (12 mm in diameter), serving as the bottom flexural reinforcement, and is connected to the top region via a steel hinge (see Fig. 2a). The centre of the GFRP bar is positioned 50 mm from the bottom edge of the beam. In the front central area of the right specimen, the GFRP bar is unbonded for 50 mm to prevent premature concrete failure at the central stressed edge region; in the left side of the specimen, the reinforcement is unbonded for 150 mm, with an

Table 1
Mechanical properties of concrete.

Concrete strength grade	Age (days)	Compressive strength (MPa)	Splitting strength (MPa)	Flexural strength (MPa)	Elastic modulus (GPa)
C100	28	110.4	6.8	10.1	44.8

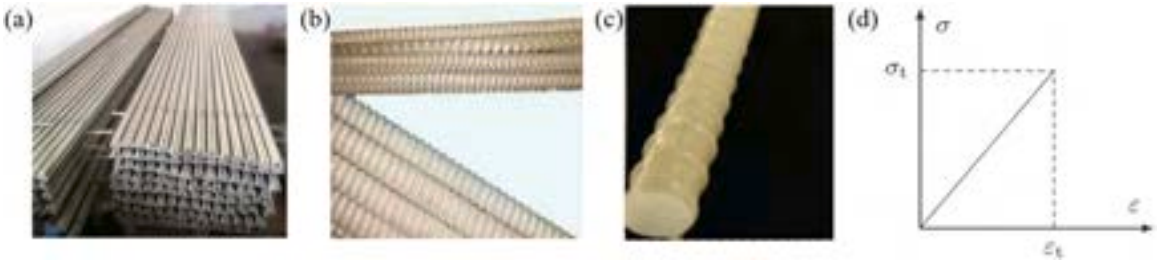

Fig. 1. Characterization of the GFRP bars: (a),(b) Overall view; (c) Close-up view of the sand-coated ribbed surface; (d) Representative tensile stress-strain curve.

Table 2
Mechanical properties of GFRP bars.

Type of the bar surface	Cross-section type	Rib spacing (mm)	Bar diameter (mm)	Ultimate strength (MPa)	Elastic modulus (GPa)
Ribs	Round	10	12	1164	56.4

embedded length of 60 mm and the free end of the bar also unbonded (Fig. 2a). The asymmetric unbonded lengths were designed to induce localized damage near the notch and to study the stick-slip mechanism under non-uniform bond conditions. Steel stirrups (HPB300 bars) with a diameter of 8 mm and a spacing of 200 mm are used. The top and bottom reinforcement consists of two steel bars, each with a diameter of 10 mm (Fig. 2b).

The test setup consists of a load actuator, a distribution beam, and steel hinge support, as shown in Fig. 3. The steel hinge supports were engineered with high-strength steel plates interconnected by 25 mm diameter precision-machined pins, as shown in Fig. 3c. This specific construction, featuring minimal clearance fits and rigid side plates, inherently provides the specified rotational stiffness of 150 kN·m/rad and a rotation capacity of ±12 °. This design ensures effectively pinned boundary conditions by allowing free rotation while maintaining precise alignment and robust axial load transfer throughout all testing stages

The specimen was placed on a four-point bending support, with the lower supports located 100 mm from the edge of the beam. The relatively short distance of 267 mm between the loading points and supports was designed to create high shear stress conditions and promote a stick-slip failure mode at the GFRP-concrete interface. A crack mouth opening displacement (CMOD) gauge was installed in the mouth notch (midpoint of the beam). Four vertical displacement gauges were placed along the bottom edge: two at the quarter-span points and two flanking the central notch. Two additional displacement gauges were positioned on the top edge, directly above the supports (see Fig. 3a). In addition, a total of two AE sensors were arranged along the GFRP arrangement direction (see Fig. 3b). A MTS loading system (100 kN actuator) was used, with the loading controlled by the CMOD. The initial loading speed was 0.05 mm/min, and it was increased to 0.2 mm/min once the crack opening reached 0.1 mm. All AE sensors, displacement gauges, CMOD, and DIC system (see Fig. 3c) were calibrated to ensure synchronised data collection. The AE system utilised is the Italy Lunitek, equipped with piezoelectric sensors (range: 10 kHz-1MHz), which are coupled via vacuum grease to the beam. The AE wave captured by the sensors is amplified with 60 dB gain before being processed, setting the acquisition threshold level up to 2 mV. Strain distribution across the specimen's front surface, particularly in the critical notch region, was captured and quantified using DIC. This provided full-field strain maps, with the analysis focused on the development of strain concentrations adjacent to the GFRP bar.

During the loading process, the DIC technique was employed for real-time recording, as shown in Fig. 3(c). Subsequently, the image analysis system was used to detect the surface displacement and calculate the full-field strain. Fig. 4 illustrates DIC speckle displacement. The reference image is divided into sub-regions, which are independently extracted and compared with the initial image to analyse the overall deformation field. Irregular speckle patterns (5~7 pixels) on the

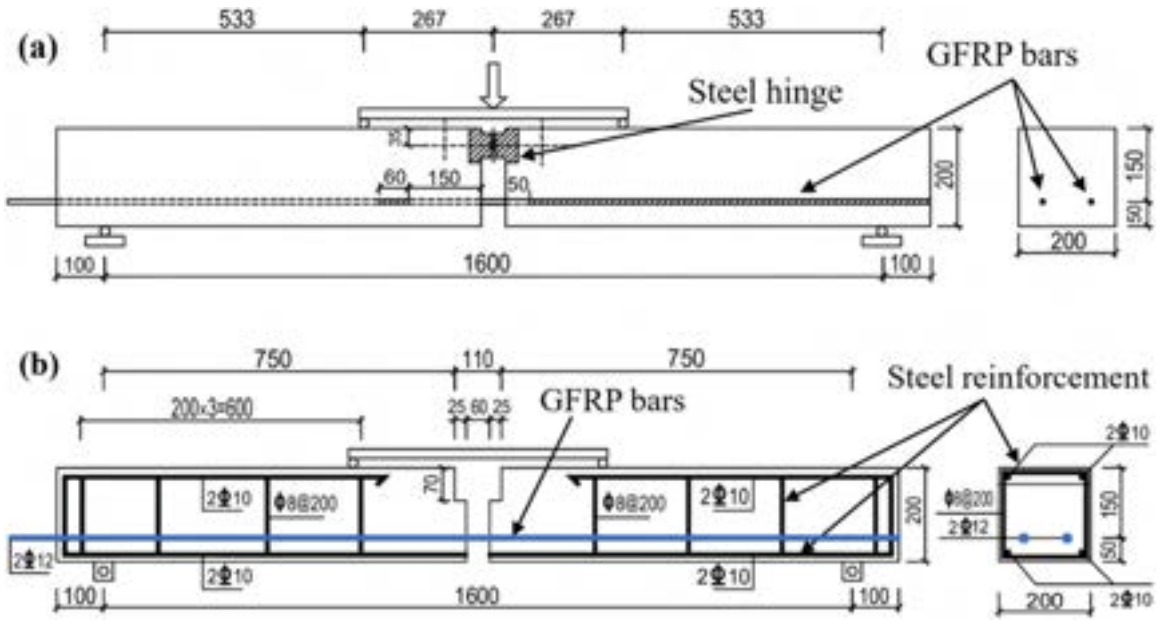

Fig. 2. Beam geometry and reinforcement (Unit: mm). (a) GFRP bars; (b) Steel reinforcement.

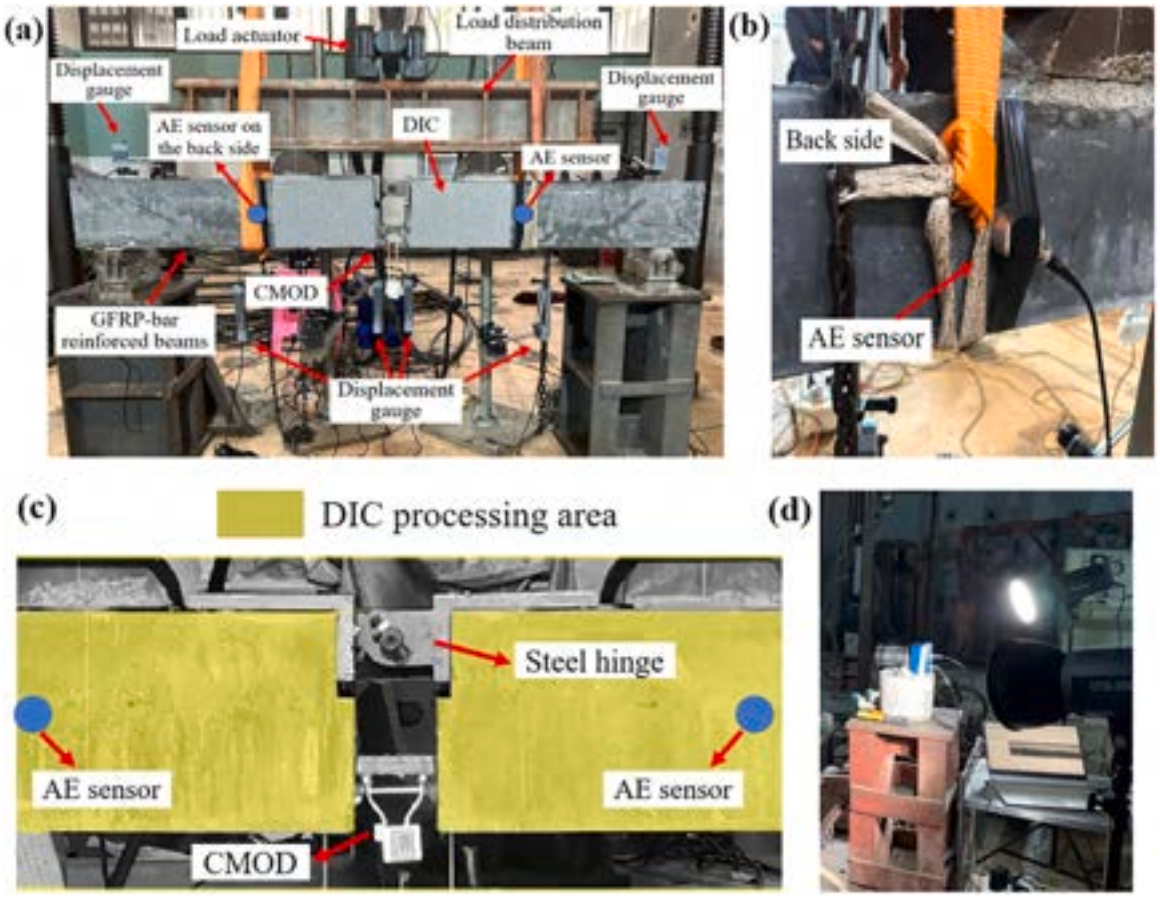

Fig. 3. Schematic of the experimental setup and instrumentation. (a) Overall testing setup, (b) detail of AE sensor, (c) DIC measurement scheme, and (d) DIC monitoring equipment.

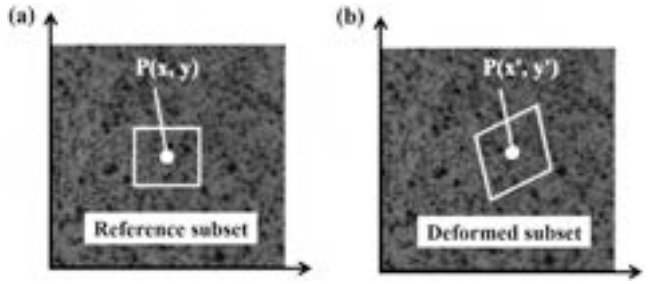

Fig. 4. Schematic of speckle displacement principle for DIC: (a) Reference subset, and (b) Deformed subset.

specimen surface enable accurate subset tracking. The tripod-mounted cameras, perpendicular to the surface, capture images during loading. The acquisition frequency is adjusted based on loading rates to record crack initiation and propagation.

While this study employs the established DIC technique for full-field analysis, other computer vision methods offer complementary damage assessment capabilities. For example, DeepLab [46] enables precise pixel-level crack identification through semantic segmentation, while EfficientNet [47] provides an efficient framework for image classification tasks such as automated damage stage or fracture mode recognition. Integrating such data-driven approaches with traditional DIC presents a promising direction for future structural health monitoring research.

2.2. Indicators of impending failure

This section describes the methodologies used to identify critical behaviour during the beam bond test, based on both global mechanical responses and AE signals. These indicators include the DPH index, Natural Time Analysis, AE Entropy, and the MCF-B approach.

2.2.1. DPH index

Debsky, Pradhan and Hansen [48] proposed a method for calculating precursors to describe the evolution of the temporal derivative of elastic energy during the system evolution, which they called the DPH index (Debski-Pradhan-Hansen index). The authors proposed that the local or global maximum of the DPH index is a precursor, and its increase is related to the significance of local or global damage in the studied system.

Fig. 5 shows the connection between this DPH index and the collapse of the system, and the calculation is shown in Eq.1. The DPH index is defined as the time derivative of the elastic energy, E, stored in the system. The evolution of the applied load, elastic energy, and the DPH index is presented in Fig. 5, represented by the black, green, and red curves, respectively. A key observation is that the peak of the DPH index occurs before the peak load. This behaviour arises because the DPH index, representing the rate of change of elastic energy, reaches its maximum when energy release through damage processes begins to surpass energy accumulation. In contrast, the load and elastic energy continue to rise until the structure attains its maximum capacity. Thus, the early peak of the DPH index provides a valuable precursor, signaling the transition toward local instability or global failure.

In literature [48], the index is calculated using numerical results, which makes it possible to study the evolution of elastic energy. In

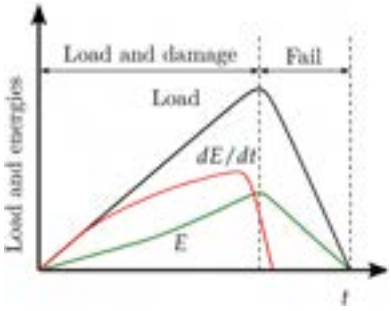

Fig. 5. Evolution of the load, elastic energy (E), and the DPH index during the test [49]. The DPH index (red curve), computed as the numerical derivative of the elastic energy (green curve), serves as a precursor to the peak load (black curve).

literature [50], this idea is generalised by considering that the product of the specified displacement of the support and the corresponding reaction force is proportional to the work done by the external forces, which is related to the elastic energy stored in the system during the test. The time derivative of this product, the DPH index, is therefore interpreted as a proxy for the rate of change of this stored energy. It serves as a robust qualitative indicator of intense energy release and irreversible damage events, rather than providing an absolute measure of the true elastic energy. When applying AE tests, the DPH index is used as supplementary information to interpret the AE data and thus analyse the damage process [49,51,52].

$$\text{DPH Index} = \frac{dE}{dt} \tag{1}$$

2.2.2. Natural time analysis

Natural Time analysis provides a method to predict when a complex system enters a critical state [53,54]. Varotsos et al. [55,56] illustrated the effectiveness of the natural time analysis in systems approaching critical conditions, underscoring its relevance across multiple domains. Additionally, numerous researchers have implemented this approach in the analysis of AE signals [57–59]. This method is based on the time-series analysis of N events represented in a specific time domain, namely the natural time, χ. The variance κ_1 of the natural time is defined as:

$$\kappa_1 = \sum_{k=1}^{N} p_k \chi_k^{\,2} - \left(\sum_{k=1}^{N} p_k \chi_k\right)^2 = \langle \chi^2 \rangle - \langle \chi \rangle^2 \tag{2}$$

where $\chi_K = K/N$ is a normalized order of occurrence of the K-th event, and $P_K = Q_K / \sum_{i=1}^{N} Q_i$ is a probability distribution of the discrete variable χ_K. The parameter Q_k can denote various physical quantities depending on the type of time series. For instance, Q_k could be interpreted as AE energy, the rise angle, or signal amplitude [60–62]. When κ_1 converges to 0.07, the damage process is said to be close to the critical state [63].

In particular, two conditions have been defined for identifying the transition of the monitored structure to a critical state [64]:

(I) The parameter κ_1 is approaching the value 0.07 "by descending from above";

(II) The entropies S and S_{rev} are lower than the entropy of the uniform noise, which is $S_u = 0.0966$. The entropy S is defined as:

$$s = \langle \chi \ln \chi \rangle - \langle \chi \rangle \ln \langle \chi \rangle, \text{where} \langle \chi \ln \chi \rangle = \sum_{k=1}^{N} \chi_k \ln \chi_k \tag{3}$$

Similarly, the entropy S_{rev} is obtained by considering the time reversal $T_{PK} = P_{N,K+1}$.

Therefore, when the critical conditions (I) and (II) are satisfied, the time is found, at which the first fracturing occurs in the monitored structure.

2.2.3. AE entropy analysis

The AE entropy performed more efficiently compared to the other conventional AE parameters on account of its being independent of threshold, and being more sensitive to changes in AE signal irregularities [65–67]. Conventional AE parameters such as amplitude, energy, duration, rise time, counts to peak, etc., have been used in the past to study fracture of concrete. These parameters have their own limitations [68].

Information entropy, initially introduced by Claude E. Shannon, seems to overcome these limitations. It was first introduced in 1948 by the name of information entropy [69]. Santo et al. [70] observed that with increasing threshold value the different AE parameters, namely, AE energy, count, duration, and rise time, were reduced. Only AE entropy and amplitude were found to be independent of threshold; but unlike amplitude, AE entropy carried the necessary information to predict the waveform characteristics. Change in hit definition time was also found to affect all the AE parameters except entropy. Using AE entropy, Kahirdeh et al. [71] could identify three distinct stages of damage in composites.

AE waves generated during the initiation and propagation of cracks in a beam subjected to flexural loading will have a unique disorder in its waveform. This can be quantified to identify the different damage stages. One way of achieving it is by obtaining the probability distribution of the waveform's discrete voltage value, termed as information entropy [70].

The information entropy or Shannon entropy is given by:

$$H = -c \sum_{i=1}^{n} p(x_i) * \log(p(x_i)) \tag{4}$$

where, x_1, x_2, x_3, …x_n are a given random sequence. $p(x_i)$ is its associated probability mass. H is the non-negative Shannon entropy. C is an arbitrary positive constant being equal to 1/log(2). The unit of its measurement is in bits.

2.2.4. The novel MCF-based (MCF-B) approach

The classical b-value is a widely employed parameter in seismology and AE studies to characterise the frequency-magnitude distribution of events. It is based on the Gutenberg-Richter empirical law, which assumes a power-law relationship between the number of events N with magnitude greater than M:

$$\log N(A) = a - bM \tag{5}$$

where a and b are empirical constants, and b reflects the relative occurrence of small versus large events. Nevertheless, in many practical situations, the frequency-magnitude relationship deviates from a pure power law, limiting the applicability and interpretability of the classical b-value. Such deviations often occur in complex or evolving systems, where underlying physical mechanisms may cause changes in the scaling behaviour of event sizes [72,73]. To overcome these limitations, the Method of Critical Fluctuations based approach (MCF-B) has been proposed [74].

The MCF-B approach introduces two competing decay exponents in the distribution of AE magnitudes, allowing for greater flexibility in capturing deviations from power-law behaviour. More precisely, the frequency-magnitude relationship is described as:

$$N(A) = \quad p_1 \cdot A^{-p_2} \quad \cdot e^{-Ap_3} \tag{6}$$

being p_1 a constant, p_2 a power-law decay exponent and p_3 an exponential decay exponent. Both p_2 and p_3 are able to take into account deviations from data linearity in the same way as in the original MCF and therefore this proposed method is called "based" [74].

The introduction of the exponential decay term p_3, alongside the traditional power-law exponent p_2, constitutes the core innovation of the MCF-B method. This dual-exponent model specifically addresses a

fundamental limitation of the classical *b*-value by effectively capturing the prevalent deviations from linearity in the frequency-magnitude distribution, thereby offering a more robust and physically nuanced precursor.

The proposed MCF-B method follows the three main steps below [74]:

(a) Calculate the histogram of the AE amplitude for an initial data set, *B*, always starting at event number 1; that is, a time series starting from event #1 to # *B* is considered.

(b) Plot each obtained distribution *N*(A) on a log-log plot. Fit the distribution using the function presented in Eq. (8) to determine a set of exponents p_2 and p_3.

(c) For each new event in the time series, perform steps 1 and 2 again; that is, a time series starting from event #1 to #*B*+ 1 will be considered. This led to the rescaling of exponents p_2 and p_3 up to the end of the AE data.

In the MCF-B approach, criticality is identified by the evolution of the fitting exponents p_2 and p_3 in the amplitude distribution. A system approaching failure typically exhibits [74]:

(1) The presence of a "perfect" power law (that is $p_2 > 1$ and $p_3 \approx 0$);

(2) Followed by the decrease of p_2 and the monotonic increase of p_3.

In fact, the behaviour of the exponents of the MCF-B approach reveals a crossover phenomenon when the system is close to failure.

2.3. Morphological AE analysis via RA-AF method

In order to complement the statistical indicators of criticality (DPH, AE Entropy, MCF-B, and Natural Time), *RA-AF* analysis was employed to explore potential transitions in fracture modes during the beam bond test. The *RA-AF* method classifies AE events based on waveform morphology based on two signal parameters Rise Angle (*RA*) and Average Frequency (*AF*) [75,76], defined as:

$$AF = \frac{RC(Ringing\ Count)}{DT(Duration\ Time)} \tag{7}$$

$$RA = \frac{RT(RiseTime)}{A_{\max}(Amplitude)} \tag{8}$$

where *RC* represents the number of signal oscillations greater than the AE threshold, *DT* is the time elapsed between the first and the last signal oscillation above the AE threshold, *RT* is the time between the first signal oscillation crossing the threshold and the maximum signal amplitude, and $A_{\max}$ is the peak amplitude of the AE signal. *AF* is measured in kHz, whereas *RA* is measured in ms/V. Following the RILEM Recommendations, tensile cracks (Mode I) are characterised by higher *AF* and lower *RA* values, whereas shear cracks (Mode II) are characterised by relatively low *AF* and high *RA* values [77], as shown in Fig. 6b.

3. Results and discussion

3.1. Global behaviour and failure configuration

Fig. 7 presents the load-time curves of the three test beam from the same batch, the normalized time of 1 corresponds to the peak load. As shown in Table 3, the average peak load of the three beams is 101.4 kN. The three beams exhibited low dispersion (CV = 2.30 %), indicating stable load-bearing performance and well-controlled loading conditions for this investigative study. Therefore, the subsequent AE monitoring focused on Specimen 1, whose peak load was closest to the mean value, for a detailed, multi-technique analysis of the damage process.

It is noteworthy that saw-tooth-shaped load drops were observed prior to reaching the peak load. Given the high strength of the concrete matrix, this indicates the occurrence of stick-slip behaviour between the GFRP bars and the concrete matrix, as marked in Fig. 7.

The stars in Fig. 7 indicate the time at which specimens 1–3 were analysed for DIC images, which will be discussed later in Fig. 9.

The observed stick-slip behaviour is indicative of the bond-slip mechanism between the GFRP bars and the concrete matrix. Initially, the bond is maintained through mechanical interlocking and friction provided by the ribbed surface of the GFRP bars. As loading progresses, localized debonding occurs, leading to sudden load drops. Each drop corresponds to a slip event, during which the bar partially disengages from the concrete, followed by re-engagement as the load redistributes.

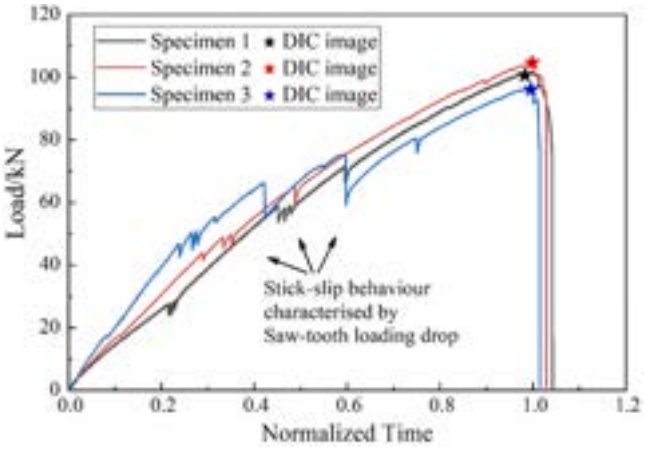

Fig. 7. Global behaviours of the test beams.

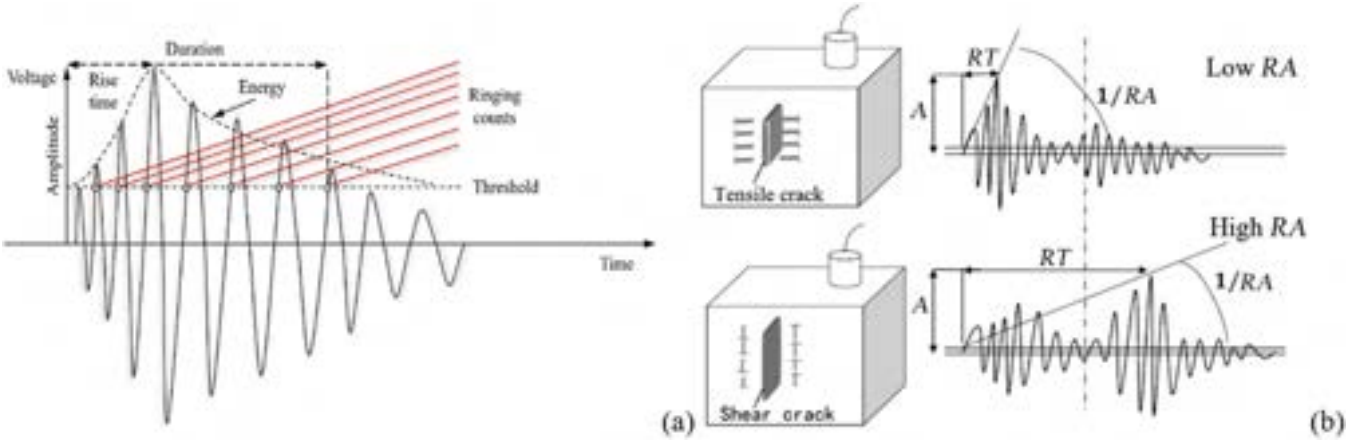

Fig. 6. Tensile (Mode I) and shear (Mode II) cracks. (a) AE waveform parameters; (b) Crack type.

Table 3
Mechanical responses of the test beams.

Beam number	Peak load /kN	Average peak load /kN	Standard deviation	Coefficient of variation	Range
Specimen 1	101.2	101.4	2.33	2.3 %	5.6 %
Specimen 2	104.3				
Specimen 3	98.6				

This process is accompanied by shear-dominated cracking near the bar-concrete interface.

Fig. 8 illustrates the final failure pattern of Specimen 1–3, characterised by transverse shear cracks distributed across its faces (Fig. 8a). Upon inspecting the interface between the GFRP bars (see Fig. 8b) and the concrete, pull-out failure was identified. The sand coating on the GFRP bars had been entirely sheared off along the full length of the embedment. The bond failure of the GFRP bars occurred partially along the bar surface and partially within the surrounding concrete, where the external sand-coated surface of the bar had been locally sheared off. The specimen did not experience complete failure due to the controlled loading, which only reached the material's normal compressive strength. Therefore, the subsequent analysis assumes the potential for imminent failure of the specimen towards the peak load. It is worth noting that the failure of the three specimens in Fig. 8 is caused by the horizontal shear crack near the GFRP bars in the notch, which is consistent with the sudden drop after the peak load in Fig. 8.

The calculation results of DIC for the three specimens are shown in Fig. 9. Since the crack morphology is predominantly horizontal, the equivalent strain field and the horizontal strain field are presented.

The equivalent strain field diagrams show that the cracks are mainly concentrated near the GFRP bars in the notch area. In addition, the horizontal strain field diagram in Fig. 9 reveals the morphology of the horizontal cracks, which is consistent with the final failure configuration in Fig. 8.

3.2. AE activity and RA-AF analysis

The loading history and AE behaviour of Specimen 1, including cumulated AE signals and the AE amplitudes, are illustrated in Fig. 10(a) for Sensor 1 and Fig. 10(b) for Sensor 2. In both figures, the load curve is plotted against the left vertical axis, while the normalized AE amplitudes are displayed on the right axis, with A_{max} denoting the maximum amplitude recorded between the two sensors. The horizontal axis represents normalized time, where $t = 1$ corresponds to the peak load. A comparison of AE amplitudes reveals that the maximum amplitude detected on the left side (Sensor 1) was significantly higher than that on the right side (Sensor 2), suggesting more intense AE activity on the left. Furthermore, Sensor 1 registered a greater number of AE signals compared to Sensor 2. These observations align with the final damage configuration depicted in Figs. 8 and 9, which clearly show damage localisation on the left side of Specimen 1. The pronounced AE activity on the left side may be associated with the propagation of transverse crack tips.

The cumulated AE curve reveals a stable growth rate in the initial loading stage, followed by a sharp rise in AE signal activity immediately prior to peak load, signalling the onset of impending failure.

Due to the relatively high strength of the concrete matrix in the GFRP-bar reinforced beams, early-stage cracking is unlikely. The load-time curve exhibits a distinct "saw-tooth" pattern during loading,

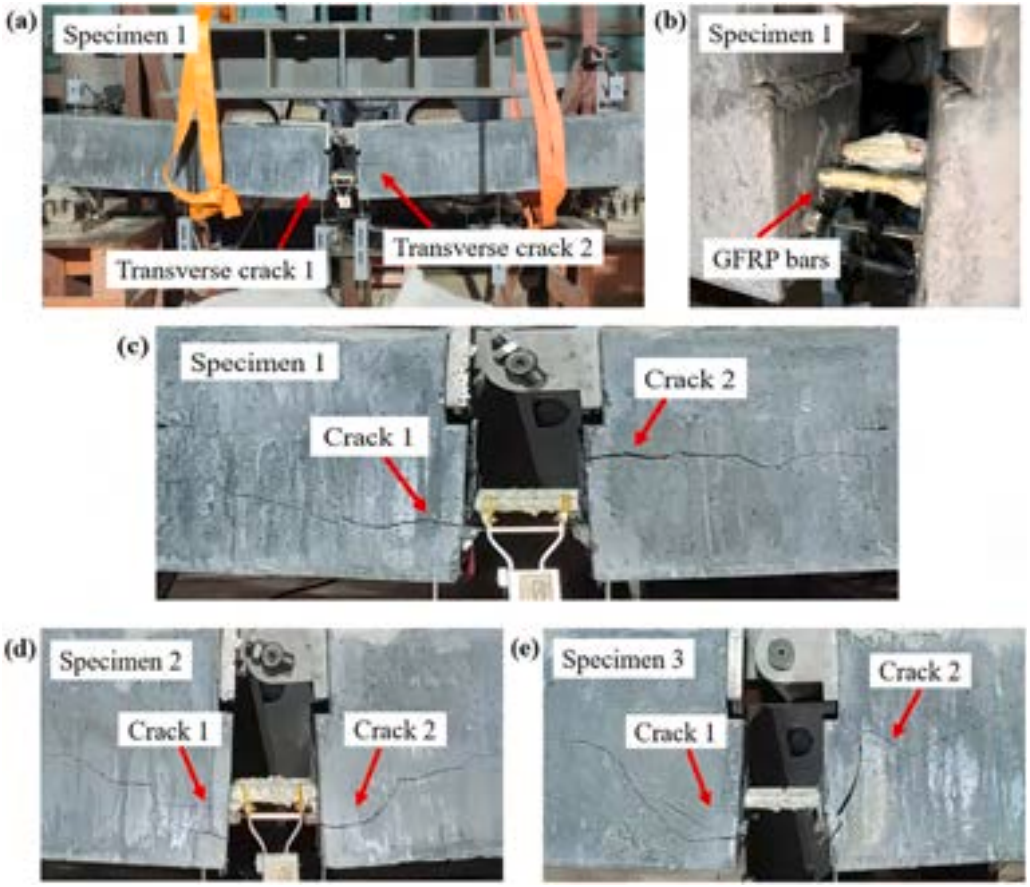

Fig. 8. Final failure configuration and details. (a) Final failure of Specimen 1; (b) Failure of the GFRP bars in Specimen 1; (c-e) Details of Specimen 1–3.

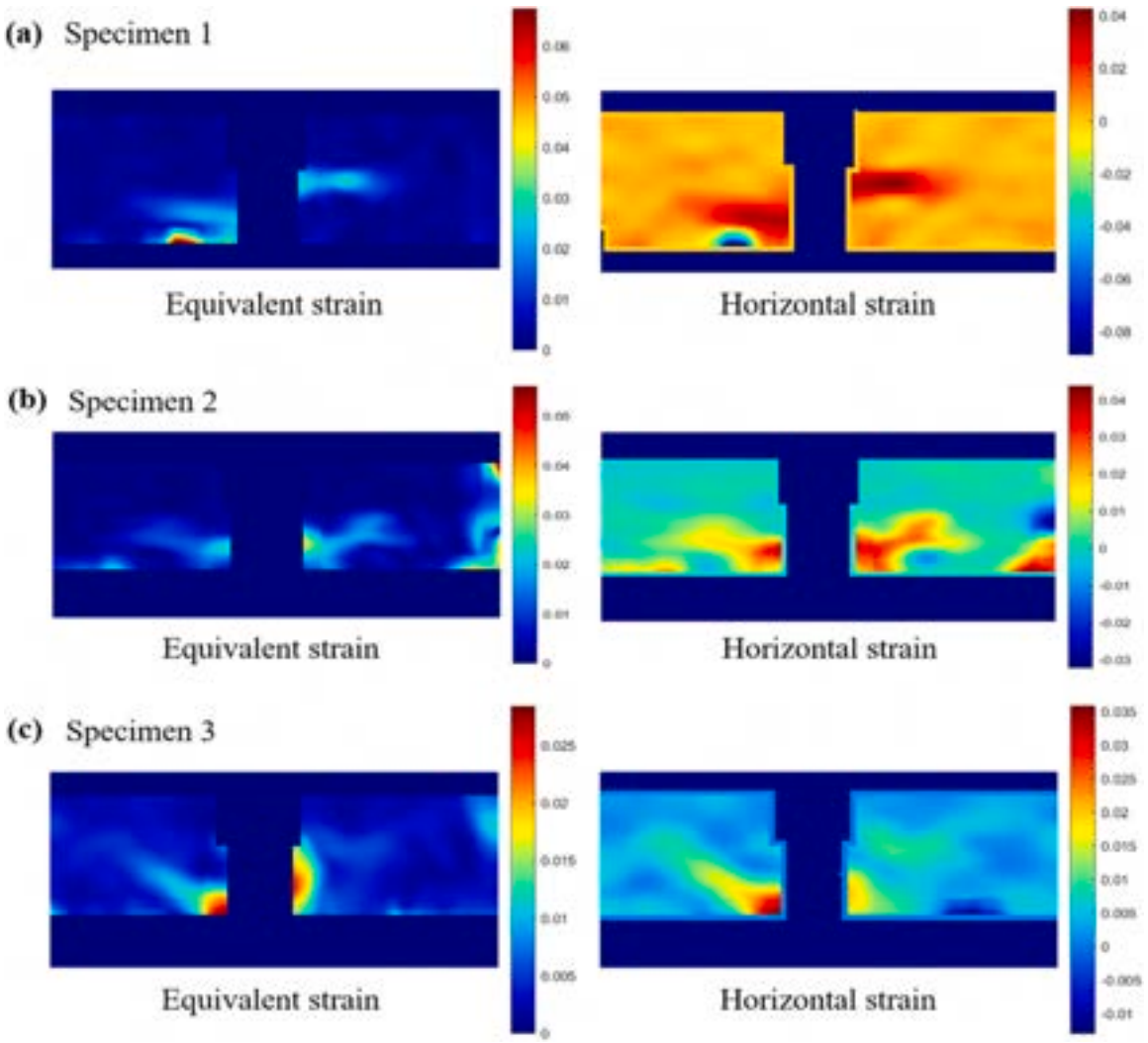

Fig. 9. DIC strain field diagram at the final failure of Specimen 1–3.

indicative of stick-slip behaviour associated with GFRP bar debonding from the concrete. Notably, these "saw-tooth" features coincide with peak AE signal amplitudes, which occur slightly before the stick-slip behaviour, reflecting heightened AE activity at this stage. As illustrated in Fig. 10c, a strong correlation exists between GFRP-bar stick-slip and AE amplitude peaks, with each load drop corresponding to an AE amplitude peak. Specifically, three load drops align with three AE amplitude peaks in Case 1 (Fig. 10c), while a single load drop corresponds to one AE amplitude peak in Case 2 (Fig. 10c). These observations suggest that AE amplitude peaks can be an indicative to identify the stick-slip ocurrency between the GFRP bars and the concrete.

It is worth mentioning that although both AE sensors were active during data acquisition, each sensor was positioned to monitor a different half of the split beam, effectively corresponding to distinct structural domains. From a methodological standpoint, AE signal analysis should ideally be performed using data from a single sensor—specifically, sensor 1—to avoid confusion with signals originating from mechanically decoupled regions. However, the number of AE events recorded by sensor 2 was significantly lower compared to sensor 1. Consequently, its contribution to the overall data set is negligible, and its inclusion is not expected to substantially affect the interpretation of the results. For this reason, and to preserve the integrity of the original signal processing workflow, the full data set was retained in the current analysis. Future studies may benefit from a more segregated treatment of sensor data, allowing for a more accurate spatial characterisation of damage mechanisms and their propagation paths through distinct material interfaces. From this point, the subsequent AE parameter analysis will be based on the data from both Sensor 1 and Sensor 2, as presented in Fig. 10c.

The correlation between AE amplitude peaks and load drops underscores the role of AE in capturing the bond-slip mechanism. Each slip event releases elastic energy, generating high-amplitude AE signals. The progressive increase in shear crack proportion (see Fig. 12 below) further supports the interpretation that bond degradation is driven by shear-induced debonding along the bar interface.

As shown in Fig. 11a, a window with a normalized time of 0.15, namely Stage SS1 and SS2, was used to identify the stick-slip behaviour via *AF-RA* analysis, respectively. Besides, the damage process before the peak load was divided into three stages (TS1, TS2, TS3) by stick-slip points, with *AF-RA* analysis performed for the above three stages.

Fig. 12 presents the percentage distribution (%) of shear cracks (Mode II) versus tensile cracks (Mode I) during stick-slip behaviours and different damage stages. As shown in Fig. 12a, shear cracks dominate the two stick-slip stages, accounting for 62 % and 70 % of total cracks respectively, clearly demonstrating shear-dominated cracking behaviour during these phases.

The damage progression, segmented by stick-slip points, reveals distinct cracking patterns across stages (Fig. 12b,c). In Stage TS1, approximately 80 % of newly formed microcracks exhibit tensile characteristics. Stage TS2 marks a significant shift, with a substantial

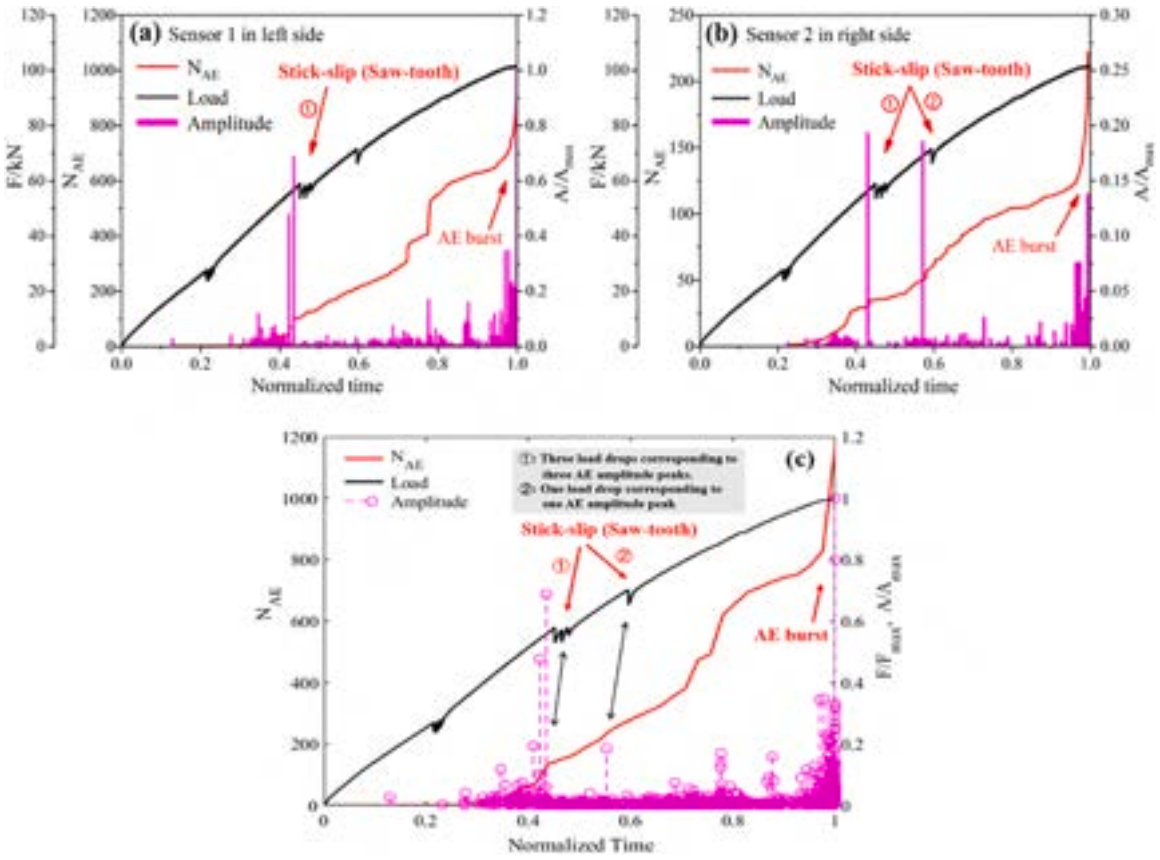

Fig. 10. Comparison of AE signals on the left and right sides of the test beam. (a) Sensor 1 on the left side; (b) Sensor 2 on the right side (c) Both Sensors 1 and 2.

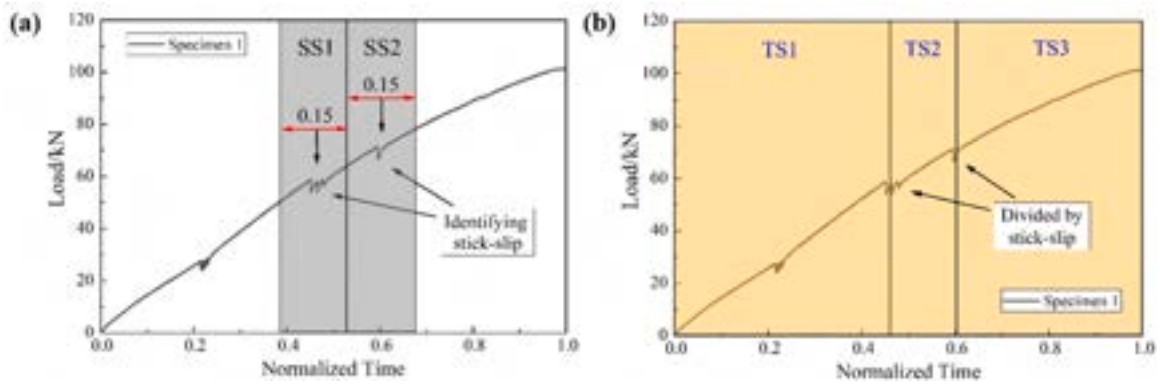

Fig. 11. Damage stage divisions for *AF-RA* analysis. (a) Two divisions for identifying the stick-slip and (b) Three divisions for damage process.

increase in shear crack formation that alters the failure mode from tension-dominated to shear-dominated - a transition consistent with the stick-slip behaviour observed in Fig. 11b. This trend culminates in Stage TS3, where shear cracks predominate at a ratio of approximately 4:1 relative to tensile cracks. Notably, transverse shear cracks develop preferentially near the GFRP bar at the notch during this final stage (Fig. 9). The results systematically track this progressive transition from tensile to shear cracking (Fig. 12b), ultimately confirming that transverse shear cracking governs the final failure mechanism.

The RA-AF analysis classifies crack types based on acquired AE signals. Although the limited number of sensors prevents precise source localization, the identified dominance of shear cracks during stick-slip is strongly corroborated by complementary evidence. DIC results in Fig. 9 show damage localization in the notch region, and the final failure in Fig. 8 confirms a shear-driven pull-out at the GFRP-concrete interface. This consistency across techniques confirms that the RA-AF results reliably reflect the dominant fracture mode in the active damage zone.

3.3. Criticality indicators

This section presents the evolution of statistical indicators used to characterise critical behaviour during the beam test. These include methodologies based on both global mechanical responses and AE signals. Each of these metrics aims to capture different aspects of the transition from stable microcracking to imminent structural failure.

3.3.1. DPH index

The curve in Fig. 13 shows the variation of the DPH index (Specimen 1, 2 and 3), and the red star indicates the maximum value of the DPH index. It is important to note that, although this section focuses on the

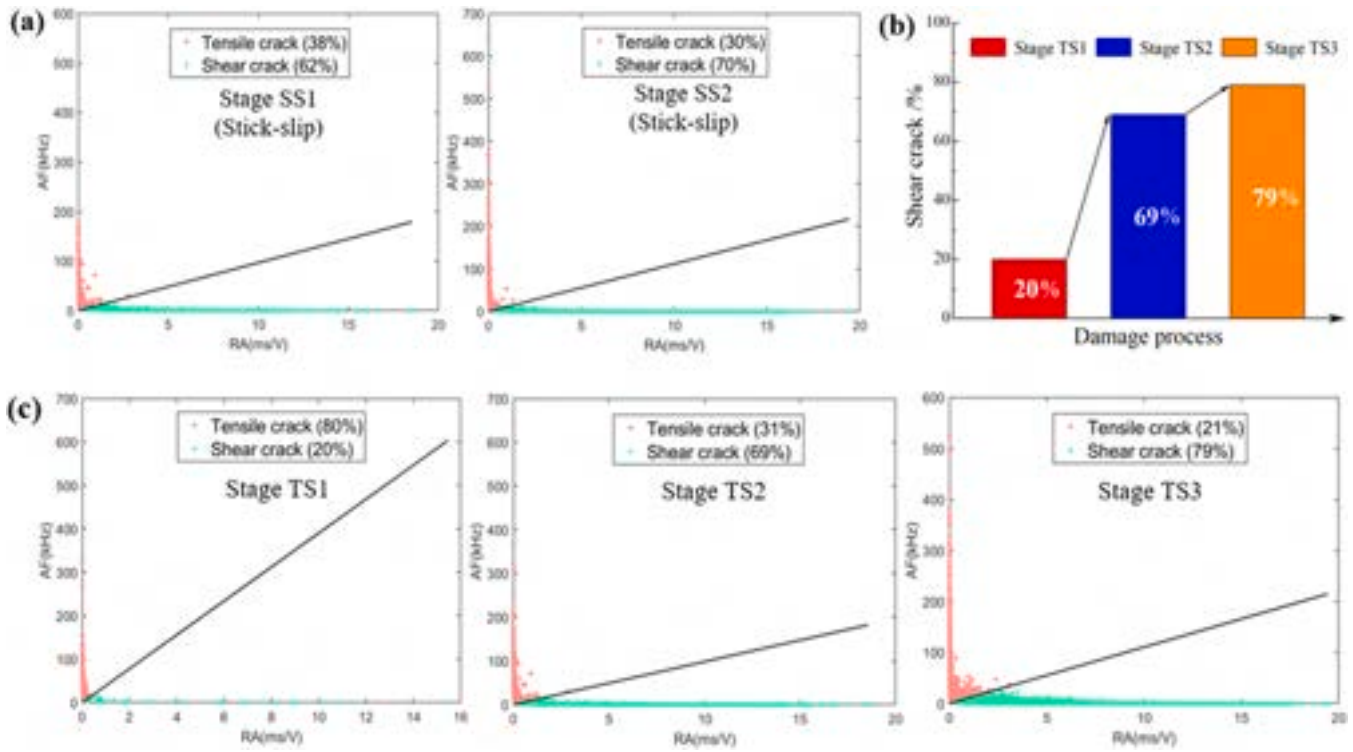

Fig. 12. Mode I and Mode II crack openings during the damage process. (a) Results for two stick-slip stages; (b,c) Results for three different damage stages.

analysis of the results from Specimen 1, Fig. 13 presents the DPH index for all samples to demonstrate the robustness of the approach. The DPH index was calculated using a moving average in a window of 200 values to reduce fluctuations while preserving the overall trend. As described in literature [49,50], this maximum value can be considered as a supplementary precursor to collapse when performing AE tests.

It should be noted that in the experimental case, the support reaction load (shown in Fig. 3) multiplied by the prescribed displacement is considered as a measure related to the mechanical work input, and its time derivative, the DPH index, is calculated based on this value [49]. As clarified in Section 2.2.1, this approach provides a proportional indicator of the global energy rate changes rather than a direct conversion to the precise elastic energy within the specimen. In the test, the maximum value of the DPH index seems to be closely related to the local cracking (stick-slip shown in Fig. 7) during the test.

In this study, the DPH index was developed as an indicator capable of detecting both local and global instability. As demonstrated in Fig. 13a-c, the local maxima (highlighted in yellow regions) exhibit predictive capability for forthcoming alterations in the specimen's global mechanical response (yellow circles). The temporal evolution of the index reveals a consistent pattern: each local maximum is succeeded by a transient decrease in the index value, followed by a substantial increase.

3.3.2. *Natural time analysis results*

Some important features related to the damaging process can be deduced from the natural time analysis, which returns the variance κ_1 of the series in normalized time. In Fig. 14a, the evolution of κ_1, S, and S_{rev} of the natural time series $\{\chi_k\}$ is shown considering a window size of 100, and the natural time parameters Q employs the AE energy. The two horizontal dotted lines represent the critical value of the variance, $\kappa_1 = 0.07$, and the critical value of the entropy, $S_u = 0.0966$.

For the natural time results, Fig. 14a shows that it can identify a single critical region (highlighted with a grey background), situated near 0.65 of the normalized time, and the critical area occurs before the peak load.

3.3.3. *AE entropy analysis results*

Each AE waveform generated during a damage progression will have a unique disorder, and the measure of this disorder could be used to identify the various stages of damage in a material [78]. The discrete voltage value of a waveform provides its probability distribution which can be quantified as information entropy. The different failure stages of a beam in bending tests can be identified by analyzing the variation curve of AE entropy.

In the calculation of AE entropy, the cumulative window is used to calculate the entropy of the AE time series with a window size of 50, and the results are shown in Fig. 14b. The initial entropy reduction (Fig. 14b) likely reflects stress localisation and temporary stabilisation within the beam structure [79,80]. Subsequent loading induces crack propagation, generating localised stress concentrations and nonlinear mechanical responses. As shown in grey area of Fig. 14, low entropy (minimum) indicates a more ordered state in the system, suggesting that the structure is prepared for impending failure (either local or global). Beyond this stage, progressive structural instability manifests through localised fracture events and plastic deformation, driving a sharp entropy increase. The AE entropy ultimately peaks near 1.2, reflecting a highly disordered post-critical state. Notably, these entropy fluctuations exhibit strong temporal correlation with AE burst activity. The identified low-entropy regime (grey region, Fig. 14b) corresponds precisely to the critical zone determined via Natural Time Analysis (Fig. 14a), where entropies must be low to indicate approaching criticality.

3.3.4. *MCF-B analysis results*

Fig. 14c illustrates the outcomes of employing the MCF-B method on the AE time series derived from the acquisition system, with all plots utilizing normalized time. The exponents p_2 and p_3 are calculated using a moving window of events, W, set to 50 events, by adding event by event throughout the normalized testing period. These exponents are computed at event #W, while the time series is initiated from event #1. The series then advances through event #2 to #W + 1, event #3 to #W + 2, and so on. The estimation of the above exponents is based on the fitting function described in Eq. (6).

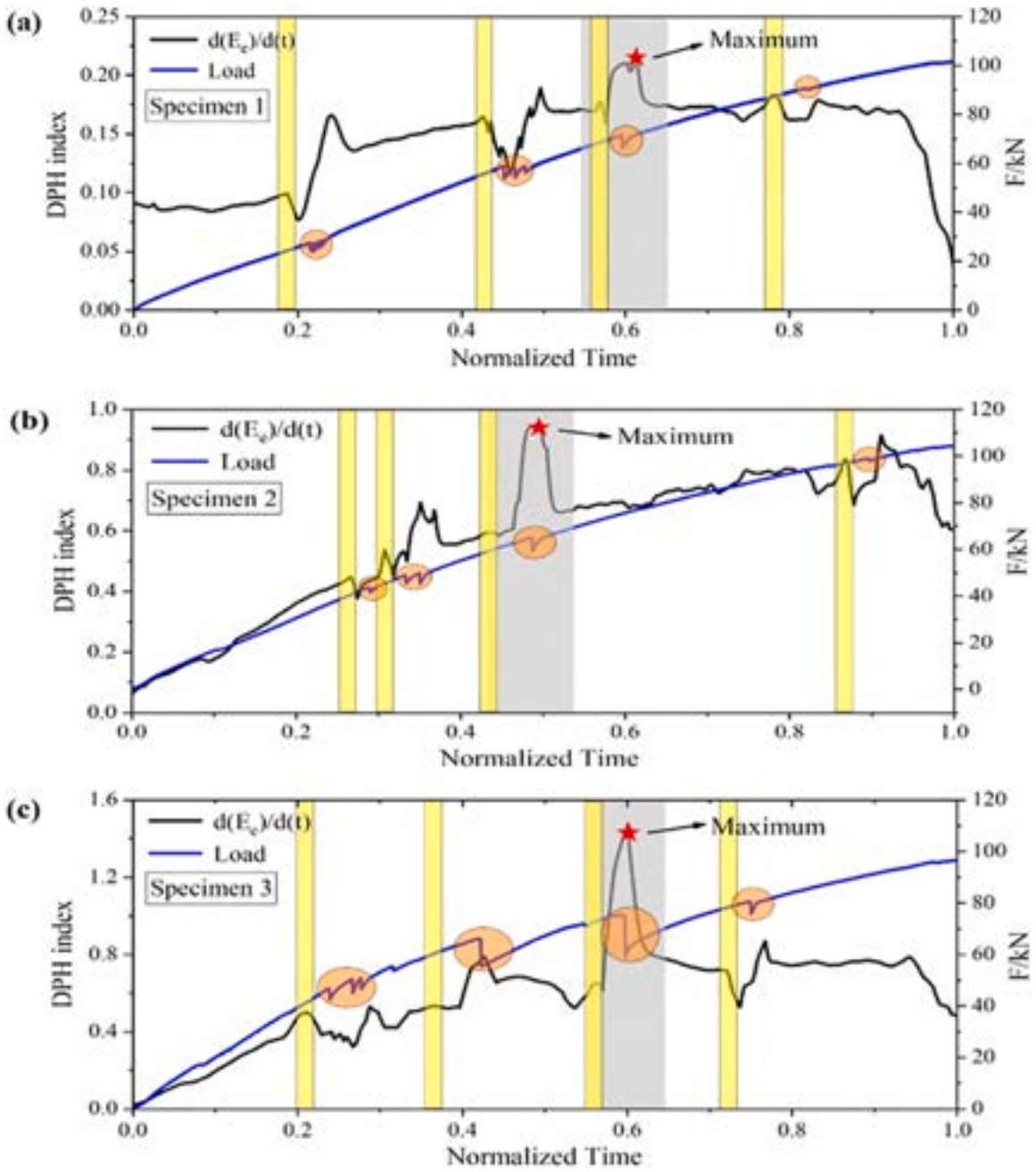

Fig. 13. (a)-(c) results for Specimens in terms of DPH index evolution. The load in plotted together (on the right-hand scale).

A characteristic of the MCF-B method that signals the system is in a critical state (grey background area, Fig. 14c) can be defined as follows: the presence of a minimum value of p_3 and then, simultaneously, the decrease of p_2 and the monotonic increase of p_3, as indicated by the black dotted box in Fig. 14c. After this critical state, the beam failure occurred. In Fig. 14c, when the distribution is characterised by $p_2 > 1$ and $p_3 = 0$, a perfect correlation is observed between the power law and the fitted curve. A is the signal peak amplitude, and N_{AE} is the number of AE events with magnitude greater than M, where $M = \log_{10}(A_{max})$.

In addition, it can be found that the critical regions identified by Natural Time Analysis (Fig. 14a) and MCF-B method (Fig. 14c) are consistent. This result opens up the possibility of applying the MCF-B method for detecting and analysing failure precursors in structures.

3.3.5. *Comparison between MCF-B and b-value*

To directly evaluate the performance of the novel MCF-B method against the traditional b-value analysis, a dedicated comparison is presented in this section. Fig. 15 shows the results of the b-value under normalized time, together with the analysis of MCF-B. In this study, the temporal variation of the b-value was estimated using a moving event window method, with a window of 100 events and a step of 50 events. This direct juxtaposition allows for a clear and critical evaluation of the novel method against the established standard.

The criticality of MCF-B is shown in the grey area of Fig. 15. A significant decrease in the b-value was observed immediately preceding the MCF-B critical region. Notably, the minimum b-value (b_{min}) is observed at the end of the MCF-B critical region, with parameter p_2 approaching its maximum value. This inverse correlation suggests a convergence of both approaches, indicating the presence of self-similarity where events occur across all scales. It should be emphasized that MCF-B is based on a cumulative analysis approach, in contrast to the moving-window methodology employed for the b-value. Even so, the precursors are

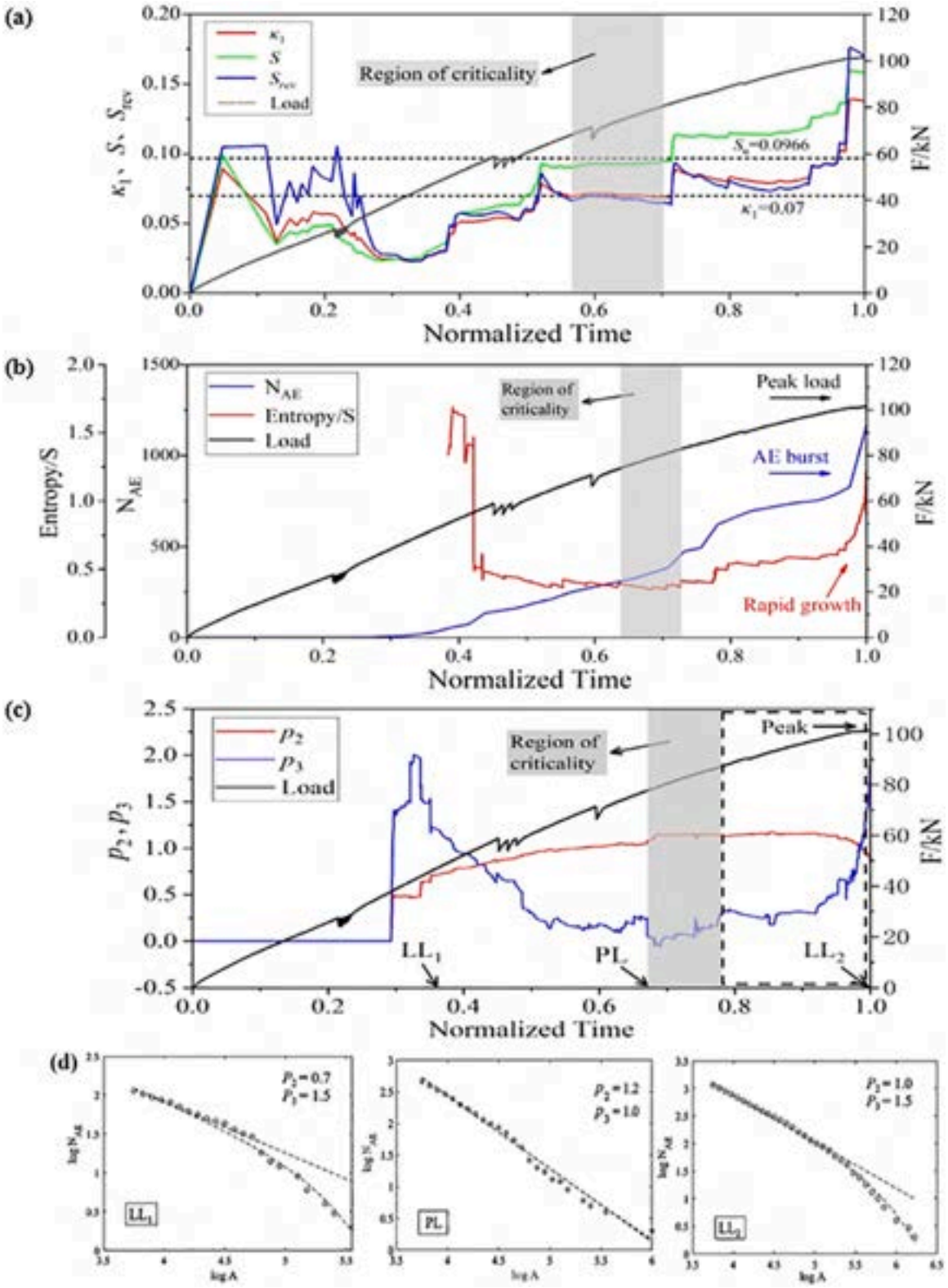

Fig. 14. Results of MCF-B, AE Entropy and Natural Time Analysis. (a) Natural Time series and its critical time; (b) AE Entropy Analysis; (c) The exponents p_2 and p_3 from MCF-B method; (d) The points that satisfy the "perfect" power law distribution labeled as PL and the loss of linearity labelled as LL_{1-2}, see the black arrows in (c).

consistent with each other. This agreement near the minimum *b*-value validates that both methods can capture the onset of criticality.

However, the most significant distinction emerges after this point. A key advantage of the MCF-B approach lies in its ability to detect increasingly larger events occurring at different scales beyond this critical point, thereby capturing the crossover phenomenon. Furthermore, within this region of $p_3 \approx 0$, the behaviour of p_2 exhibits remarkable similarity to the *b*-value evolution. Critically, while the *b*-

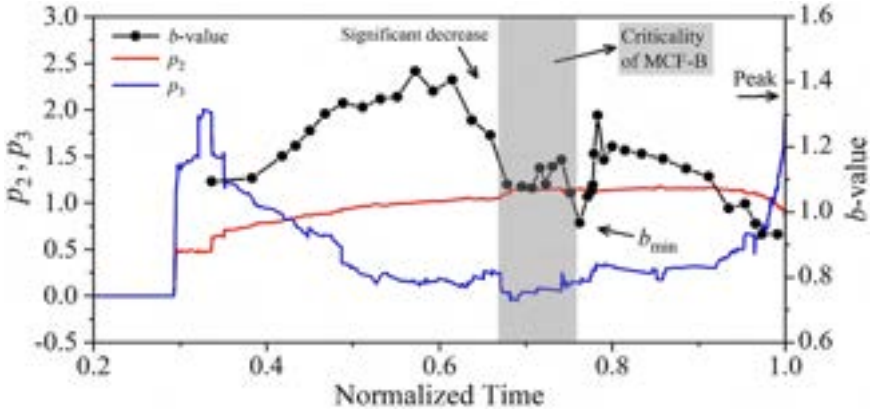

Fig. 15. *b*-value and MCF-B versus normalized time.

value may show divergent trends beyond this region, losing its clear precursory signature, the MCF-B maintains its critical signature through the systematic crossover behaviour where p_2 decreases and p_3 increases monotonically. This divergence highlights the superior robustness of the MCF-B approach for tracking the system's final approach to failure.

This enhanced performance stems from the core formulation of MCF-B, which employs a cumulative analysis and a dual-exponent model to account for deviations from power-law linearity, a limitation inherent in the classical *b*-value's single-parameter moving-window approach.

While this study focuses on comparing the MCF-B method with the classical *b*-value for clarity in introducing the new approach, a future comprehensive analysis will include benchmarking against other advanced nonlinear methods, such as the Robust Fitting Method, to further validate its performance in handling documented deviations from the Gutenberg-Richter law.

3.3.6. Overall consistency of different approaches

The convergence of MCF-B, AE Entropy, and Natural Time Analysis on a single critical region, as illustrated in Fig. 14, is a central finding of this work. This consistency is not coincidental but stems from the complementary physical principles each method captures: MCF-B reflects the scaling properties of event magnitudes, AE Entropy quantifies the disorder in signal waveforms, and Natural Time Analysis reveals the temporal organization of energy release. Their agreement provides multi-faceted and compelling evidence for the system's transition to a critical state.

All three strategies—MCF-B, AE Entropy, and Natural Time—appear to converge and identify the same critical region, thereby reinforcing the robustness of the analysis. An important observation is that, while these approaches collectively indicate a critical state, no actual rupture was observed in the specimen close to this stage, as the load continued to increase beyond the identified critical point. This behaviour highlights an important aspect of complex systems: reaching a critical state does not necessarily imply imminent rupture or collapse. For instance, in thermodynamic systems, a transition can pass through a well-defined critical regime before a phase change occurs, yet such a phase change does not inherently correspond to a destructive event. Similarly, in structural systems, a critical state may represent a reorganization of internal processes. That is, after passing through the critical regime, the structure may exhibit a modified mechanical behaviour—one that could eventually lead to catastrophic collapse, but not necessarily so.

This observed disconnect between the critical state and immediate failure directly addresses the relationship between criticality and the structure's remaining life. The critical state signifies that the material has entered a terminal phase where damage processes become strongly correlated and the risk of global failure is high. However, the remaining life is not predetermined by the critical state alone. It is determined by the system's post-critical evolution, which includes the rate of damage coalescence and the specific loading conditions. In this experiment, under displacement-controlled loading, the structure retained a finite post-critical life, allowing it to sustain further loading until the peak load was reached. The identification of the critical state thus serves as a definitive warning of impending failure, while the actual remaining operational life is the finite duration of this unstable post-critical phase.

In future work, a deeper investigation into the underlying processes within the structure at the identified critical stage should be conducted. This may include the application of AE-based source localization techniques to determine the spatial distribution of emission sources, as well as the integration of complementary monitoring methods to better characterize the nature and evolution of the observed criticality.

3.4. Discussion on bond-slip mechanism

The experimental results provide clear insight into the bond-slip mechanism in GFRP-bar reinforced concrete beams. The stick-slip behaviour observed in the load-time response is a direct manifestation of the intermittent loss and recovery of bond at the bar-concrete interface. This behaviour arises from the competing actions of frictional resistance and mechanical interlocking provided by the ribbed bar surface. As the applied load increases, shear stresses at the interface exceed the local bond capacity, leading to sudden slip events. These events are accompanied by acoustic emission bursts and a shift in cracking mode from tensile to shear, as evidenced by RA-AF analysis. The final failure involves shearing of the sand-coated layer and partial bar pull-out, confirming that stick-slip is a shear-dominated process. These findings highlight the importance of interfacial characteristics in the design of GFRP-reinforced concrete structures.

3.5. Comparison with previous studies

The damage process and failure mechanisms observed in the GFRP-bar reinforced concrete beams of this study are consistent with several key findings from prior research. The dominant failure mode of transverse shear cracking near the notch area, coupled with GFRP bar pull-out failure observed in this work, aligns with the bond-slip and shear-dominated failures reported in other experimental studies on GFRP-reinforced members [9,12,13]. Specifically, the complete shearing-off of the sand-coated surface along the embedment length observed in our specimens has also been noted by Kotynia et al. [12] as a characteristic bond failure mechanism for ribbed GFRP bars.

Regarding the critical failure precursors, the consistent identification of a critical region by MCF-B, Natural Time Analysis, and AE Entropy in our GFRP beam is supported by earlier studies applying these methods to quasi-brittle materials [34,58,68,74]. However, the application of MCF-B to GFRP-reinforced concrete represents a novel contribution. Its performance in maintaining a critical signature beyond the point where

the *b*-value diverges demonstrates an improvement over conventional seismic-based indicators for structural materials, as also suggested in Friedrich et al. [74].

While the overall failure modes of the GFRP beams in this study are consistent with existing literature, the multi-technical analysis combining DIC, RA-AF, and advanced AE time-series methods like MCF-B and Natural Time Analysis provides a more nuanced and robust framework for identifying impending failure, advancing the current state of structural health monitoring for GFRP-reinforced concrete structures.

3.6. Synthesis of the damage process from multi-technical analysis

The integrated analysis of DIC, AE, and statistical indices allows for a comprehensive description of the damage process. The process initiates with distributed microcracking under increasing load, evidenced by a high percentage of tensile cracks identified via RA-AF analysis in stage TS1. As loading continues, damage localizes at the GFRP bar-concrete interface, marked by the onset of stick-slip behaviour. This behaviour is characterized by synchronized load drops and AE amplitude peaks, indicating intermittent stick-slip and a transition in cracking mode from tensile to shear dominance, as shown in stages TS2 and TS3 of the RA-AF analysis.

The approach of a critical state is consistently signaled by multiple statistical indicators. The MCF-B method exhibits a characteristic signature where a perfect power law distribution is followed by a decrease in exponent p_2 and a monotonic increase in p_3. This crossover phenomenon indicates critical fluctuations in the AE time series. Concurrently, the AE Entropy reaches a minimum value, reflecting a transition to a more ordered state within the system. Furthermore, the Natural Time Analysis shows the variance κ_1 converging to 0.07. The convergence of these independent methods confirms the system's entry into a critical stage prior to the peak load.

Following this critical state, macroscopic failure ensues, dominated by the propagation of transverse shear cracks near the notch, as conclusively identified by the final DIC strain patterns and post-test observations. This multi-technical framework demonstrates that the damage process evolves from diffuse microcracking to localized interfacial damage, passes through a well-defined critical state, and culminates in shear-driven structural failure.

4. Conclusions and prospects

In this paper, AE and DIC tests were conducted on GFRP-bar reinforced concrete beams to analyse the stick-slip behaviour and failure modes during the damage process. The primary innovation of this paper lies in the novel application of the MCF-B method to the failure analysis of GFRP-bar reinforced concrete and the development of an integrated precursor identification framework. By synergistically combining statistical, entropic, and temporal analyses of AE data with global mechanical response indices, this framework demonstrates superior robustness for identifying impending failure compared to relying on any single indicator. The conclusion is as follows:

(1) A clear correlation exists between stick-slip behaviour and AE amplitudes. The AE features effectively capture the stick-slip behaviour between the GFRP bars and concrete, as evidenced by DIC-observed failure patterns and the tensile-to-shear crack transition in *RA-AF* analysis. These findings confirm that transverse shear cracks were the primary cause of final failure.

(2) A signature of the MCF-B method that indicates the system is in a critical stage is defined as: the presence of a perfect power law and then, simultaneously, the decrease of p_2 and the monotonic increase of p_3. The MCF-B analysis as a precursor is in agreement with the observations pointed out by Natural Time Analysis and AE Entropy Analysis. While the *b*-value may exhibit divergent trends beyond this critical region, MCF-B maintains its critical signature, demonstrating the robustness of this approach.

(3) Low entropy in AE Entropy Analysis indicates a more ordered state in the system—meaning the structure is prepared for failure (either local or global). In contrast, high entropy (towards 1.2 in this study) would correspond to a disordered state, farther from critical conditions. This lower entropy state aligns with the Natural Time framework, where entropies must be low to indicate approaching criticality.

(4) The evaluation of the DPH index showed that this index may indicate a maximum value close to local or global collapse, and the DPH index all reached their maximum values before the collapse occurred. Besides, the DPH index was developed as an indicator capable of detecting both local and global instability, the local maxima exhibit predictive capability for forthcoming alterations in the specimen's global mechanical response.

The current research has certain limitations. The use of only two AE sensors restricted precise spatial localization of damage sources. The findings from the specific beam configuration and material types used may not be directly generalizable. Furthermore, the advanced data analysis was conducted post-test, highlighting the need for future development of real-time monitoring systems. These aspects will be the focus of our subsequent investigations.

While this study identified critical failure precursors, it primarily focused on the analysis of AE signal patterns and their correlation with global behaviour. A direct quantification of bond strength degradation or the residual performance of the GFRP bars post-failure was not undertaken. Future work should integrate these AE-based precursor methods with direct mechanical measurements, such as detailed bond-slip constitutive law derivation from pull-out tests or residual tensile strength tests on recovered bars. This integration would bridge the gap between precursor identification and quantitative engineering parameters, further enhancing the practical value of the methodology for structural assessment.

CRediT authorship contribution statement

Zihan Jiang: Writing – original draft, Validation, Methodology, Investigation, Formal analysis, Data curation, Conceptualization. **Ediblu S. Cezar:** Writing – review & editing, Methodology, Investigation. **Jueliang Chen:** Methodology, Investigation, Conceptualization. **Zhiwen Zhu:** Methodology, Investigation, Data curation. **Leandro F. Friedrich:** Writing – review & editing, Methodology, Investigation, Formal analysis, Conceptualization. **Giuseppe Lacidogna:** Methodology, Investigation, Data curation, Conceptualization. **Ignacio Iturrioz:** Writing – review & editing, Methodology, Investigation, Conceptualization.

Declaration of Competing Interest

The authors declare that they have no known competing financial interests or personal relationships that could have appeared to influence the work reported in this paper.

Acknowledgments

The authors wish to acknowledge the National Natural Science Foundation of China (52278509), the China Scholarship Council (CSC), the Brazilian National Council for Scientific and Technological Development (CNPq), the Coordination for the Improvement of Higher Level of Education Personnel (CAPES) and the sponsorship guaranteed with basic research funds provided by Politecnico di Torino, Italy for their support in this work.

Data availability

Data will be made available on request.

References

[1] Accornero F, Cafarelli R, Carpinteri A, Nanni A. Scale effects in GFRP-bar reinforced concrete beams. Struct Concr 2023;24(2):2817–26.
[2] Zeng J, Hao Z, Liang Q, Yan Z, Liu Y. Durability assessment of GFRP bars exposed to combined accelerated aging in alkaline solution and a constant load. Eng Struct 2023;297:116990.
[3] Pan Y, Yan D. Study on the durability of GFRP bars and carbon/glass hybrid fiber reinforced polymer (HFRP) bars aged in alkaline solution. Compos Struct 2021; 261:113285.
[4] Lu C, Qi Z, Zheng Y, Xuan G, Yan Y. Long-term tensile performance of GFRP bars in loaded concrete and aggressive solutions. J Build Eng 2023;64:105587.
[5] Hosseini S, Farghaly A, Eslami A, Nanni A, Benmokrane B. Bond behaviour of lap spliced GFRP bars in concrete members: A state-of-the-art review and design recommendations. Constr Build Mater 2024;411:134714.
[6] Yang K, Wu Z, Zheng K, Shi J. Design and flexural behavior of steel fiber-reinforced concrete beams with regular oriented fibers and GFRP bars. Eng Struct 2024;309: 118073.
[7] Liao J, Zeng JJ, Bai YL, Zhang L. Bond strength of GFRP bars to high strength and ultra-high strength fiber reinforced seawater sea-sand concrete (SSC). Compos Struct 2022;281:115013.
[8] Luo Y, Liao P, Pan R, Zou J, Zhou X. Effect of bar diameter on bond performance of helically ribbed GFRP bar to UHPC. J Build Eng 2024;91:109577.
[9] Zeng JJ, Liao JJ, Zhuge Y, et al. Bond behavior between GFRP bars and seawater sea-sand fiber-reinforced ultra-high strength concrete. Eng Struct 2022;254: 113787.
[10] Romanazzi V, Leone M, Aiello MA, Pecce M. Bond behavior of geopolymer concrete with steel and GFRP bars. Compos Struct 2022;300:116150.
[11] Wu L, Xu X, Wang H, Yang J. Experimental study on bond properties between GFRP bars and self-compacting concrete. Constr Build Mater 2022;320:126186.
[12] Kotynia R, Szczech D, Kaszubska M. Bond behaviour of GRFP bars to concrete in beam test. Procedia Eng 2017;193:401–8.
[13] Ruiz Emparanza A, De Caso Y Basalo F, Kampmann R, Adarraga Usabiaga I. Evaluation of the bond-to-concrete properties of GFRP rebars in marine environment. Infrastructures 2018;3(4):44.
[14] Rundle J, Stein S, Donnellan A, Turcotte D, Klein W, Saylor C. The complex dynamics of earthquake fault systems: new approaches to forecasting and nowcasting of earthquakes. Rep Prog Phys 2021;84:076801.
[15] Venegas-Aravena P, Cordaro E. Analytical relation between b-value and electromagnetic signals in pre-macroscopic failure of rocks: insights into the Microdynamics' physics prior to earthquakes. Geosci 2023;13(6):169.
[16] Lacidogna G, Piana G, Carpinteri A. Acoustic emission and modal frequency variation in concrete specimens under four-point bending. Appl Sci 2017;7(4):339.
[17] Scholz C. The frequency-magnitude relation of microfracturing in rock and its relation to earthquakes. Bull Seismol 1968;58:399–415.
[18] Jiang Z, Zhu Z, Accornero F, Lacidogna G. Acoustic emission and digital image correlation evidence of size effects on the compression failure of concrete. Mag Concr Res 2025.
[19] Jiang Z, Zhu Z, Lacidogna G, Friedrich L, Iturrioz I. Earthquake precursors based on rock acoustic emission and deep learning. Sci 2025;7(3):103.
[20] Carpinteri A, Lacidogna G, Puzzi S. From criticality to final collapse: evolution of the "*b*-value" from 1.5 to 1.0. Chaos Solitons Fractals 2009;41:843–53.
[21] Vallianatos F, Nardi A, Carluccio R, Chiappini M. Experimental evidence of a non-extensive statistical physics behavior of electromagnetic signals emitted from rocks under stress up to fracture. *Preliminary Results*. Acta Geophys 2012;60:894–909.
[22] Iturrioz I, Lacidogna G, Carpinteri A. Acoustic emission detection in concrete specimens: experimental analysis and lattice model simulations. Int J Damage Mech 2014;23(3):327–58.
[23] Gutenberg B, Richter CF. Frequency of earthquakes in California. Bull Seismol Soc Am 1944;34:185–8.
[24] Jiang Z, Zhu Z, Accornero F, Wang C. Multi-technique analysis of seawater impact on the performance of calcium sulphoaluminate cement mortar. Constr Build Mater 2024;443:137717.
[25] Wang C, Jiang Z, Accornero F, Zhou S, Ou Q. Influence of seawater and salt ions on the properties of calcium sulfoaluminate cement. J Mater Civ Eng 2025;37(6): 04025156.
[26] Zhou S, Jiang Z, Ou Q, Liu J, Wang C. Analysis on flexural toughness of steel fiber reinforced concrete based on acoustic emission and digital image correlation techniques. Const Build Mater 2025;492:143039.
[27] Jiang Z, Zhu Z, Accornero F. Tensile-to-shear crack transition in the compression failure of steel-fibre-reinforced concrete: Insights from acoustic emission monitoring. Buildings 2024;14(7):2039.
[28] Cisternas A, Polat O, Rivera L. The Marmara Sea region: seismic behaviour in time and the likelihood of another large earthquake near Istanbul (Turkey). J Seismol 2004;8:427–37.
[29] Lee Y, Chen C, Lin C, Chi S. Negative correlation between power-law scaling and Hurst exponents in long-range connective sandpile models and real seismicity. Chaos Solit Fractals 2012;45:125–30.
[30] Friedrich L, Cezar E, Colpo A, Tanzi B, Sobczyk M, Lacidogna G, Niccolini G, Kosteski L, Iturrioz I. Long-range correlations and natural time series analyses from acoustic emission signals. Appl Sci 2022;12:1980.
[31] Varotsos P, Sarlis N, Skordas E. Spatio-temporal complexity aspects on the interrelation between seismic electric signals and seismicity. Pr Athens Acad 2001; 76:294–321.
[32] Varotsos P, Sarlis N, Skordas E. Natural time analysis: The new view of time, part II. Advances in disaster prediction using complex systems. Cham: Switzerland: Springer Nature; 2023.
[33] Zhu Z, Jiang Z, Accornero F, Carpinteri A. Correlation between seismic activity and acoustic emission on the basis of in-situ monitoring. Nat Hazard Earth Sys 2024;24 (11):4133–43.
[34] Niccolini G, Potirakis S, Lacidogna G, Borla O. Criticality hidden in acoustic emissions and in changing electrical resistance during fracture of rocks and cement-based materials. Materials 2020;13:5608.
[35] Kourkoulis S, Pasiou E, Loukidis A, Stavrakas I, Triantis D. Comparative assessment of criticality indices extracted from acoustic and electrical signals detected in marble specimens. Infrastructures 2022;7:15.
[36] Zhu Z, Jiang Z, Accornero F. Size-scale and time-scale effects on the failure of UHPC-strengthened reinforced concrete beams. Structures 2025;78:109248.
[37] Jiang Z, Zhu Z, Lacidogna G. AE monitoring of crack evolution on UHPC deck layer of a long-span cable-stayed bridge. Dev Built Environ 2025:100697.
[38] Han Q, Wang L, Xu J, Carpinteri A, Lacidogna G. A robust method to estimate the b-value of the magnitude–frequency distribution of earthquakes. Chaos Solit Fractals 2015;81:103–10.
[39] Birck G, Riera J, Iturrioz I. Numerical DEM simulation of AE in plate fracture and analogy with the frequency of seismic events in SCRs. Eng Fail Anal 2018;93: 214–23.
[40] Pradhan S, Hansen A, Hemmer P. Crossover behavior in burst avalanches: signature of imminent failure. Phys Rev Lett 2005;95:125501.
[41] Potirakis S, Contoyiannis Y, Asano T, Hayakawa M. Intermittency-induced criticality in the lower ionosphere prior to the 2016 Kumamoto earthquakes as embedded in the VLF propagation data observed at multiple stations. Tectonophysics 2018;722:422–31.
[42] Potirakis S, Contoyiannis Y, Schekotov A, Eftaxias K, Hayakawa M. Evidence of critical dynamics in various electromagnetic precursors. Eur Phys J Spec Top 2021; 230:151–77.
[43] JGJ 55-2019. Specification for mix proportion design of ordinary concrete. Beijing: Ministry of Housing and Urban Rural Development of China; 2019.
[44] GB/T 50081-2019. Standard for test methods of concrete physical and mechanical properties. Beijing: Ministry of Housing and Urban Rural Development of China; 2019.
[45] GB/T 30022-2013. Test method for basic mechanical propertiesof fiber reinforced polymer bar. Beijing, China: China Standards Press; 2013.
[46] Song Z, Zou S, Zhou W, et al. Clinically applicable histopathological diagnosis system for gastric cancer detection using deep learning. Nat Commun 2020;11(1): 4294.
[47] Kabir H, Wu J, Dahal S, Joo T, Garg N. Automated estimation of cementitious sorptivity via computer vision. Nat Commun 2024;15(1):9935.
[48] Debski W, Pradhan S, Hansen A. Criterion for imminent failure during loading—discrete element method analysis. Front Phys 2021;9:675309.
[49] Almeida W, Tanzi B, Birck G, Iturrioz I, Lacidogna G. Analysis of damage process in a pre-notched rock specimen: the synergy between experimental results and simulations using a peridynamic model. Appl Sci 2024;14(11):4721.
[50] Rojo Tanzi B, Sobczyk M, Iturrioz I, Lacidogna G. Damage evolution in quasi-brittle materials: experimental analysis by AE and numerical simulation. Appl Sci 2023; 13:10947.
[51] Jing G, Lacidogna G, Zhao Y, Montanari P, Rojo Tanzi B, Iturrioz I. Coal–rock catastrophic collapse: precursors based on ae and fiber bundle models. Int J Geomech 2025;25(1):04024314.
[52] Mayya A, Berthier E, Ponson L. How criticality meets bifurcation in compressive failure of disordered solids. Phys Rev X 2023;13(4):041014.
[53] Varotsos P, Sarlis N, Skordas E, Lazaridou M. Seismic electric signals: an additional fact showing their physical interconnection with seismicity. Tectonophysics 2013; 589:116–25.
[54] Hloupis G, Stavrakas I, Vallianatos F, Triantis D. A preliminary study for prefailure indicators in acoustic emissions using wavelets and natural-time analysis. Proc Inst Mech Eng Part L 2016;230:780–8.
[55] Varotsos C, Tzanis C, Cracknell A. Precursory signals of the major El Nino southern oscillation events. Theor Appl Clim 2016;124:903–12.
[56] Mintzelas A, Sarlis N. Minima of the fluctuations of the order parameter of seismicity and earthquake networks based on similar activity patterns. Phys A 2019;527:121293.
[57] Friedrich L, Tanzi B, Colpo A, Sobczyk M, Lacidogna G, Niccolini G, Iturrioz I. Analysis of acoustic emission activity during progressive failure in heterogeneous materials: experimental and numerical investigation. Appl Sci 2022;12(8):3918.
[58] Loukidis A, Triantis D, Stavrakas I, Pasiou E, Kourkoulis S. Detecting criticality by exploring the acoustic activity in terms of the "natural-time" concept. Appl Sci 2022;12:231.
[59] Triantis D, Stavrakas I, Loukidis A, Pasiou E, Kourkoulis S. A study on the fracture of cementitious materials in terms of the rate of acoustic emissions in the natural time domain. Appl Sci 2023;13:6261.
[60] Loukidis A, Pasiou E, Sarlis N, Triantis D. Fracture analysis of typical construction materials in natural time. Phys A Stat Mech Appl 2020;547:123831.
[61] Hloupis G, Stavrakas I, Vallianatos F, Triantis D. A preliminary study for prefailure indicators in acoustic emissions using wavelets and natural time analysis. Proc Proc Inst Mech Eng L J Mater Des Appl 2016;230(3):780–8.
[62] Niccolini G, Manuello A, Marchis E, Carpinteri A. Signal frequency distribution and natural-time analysis from acoustic emission monitoring of an arched structure in the castle of Racconigi. Nat Hazards Earth Syst Sci 2017;1025:1032.

[63] Vallianatos F, Michas G, Benson P, Sammonds P. Natural-time analysis of critical phenomena: the case of acoustic emissions in triaxially deformed etna basalt. Phys A 2013;392(20):5172–8.
[64] Hloupis G, Stavrakas I, Pasiou E, Triantis D, Kourkoulis S. Natural-time analysis of acoustic emissions in double edge notched tension (DENT) marble specimens. Procedia Eng 2015;109:248–56.
[65] Samal D, Ray S. Wavelet entropy-based damage characterization and material phase differentiation in concrete using acoustic emissions. Eng Fail Anal 2024;160:108144.
[66] Chang X, Wu S, Wang J, Fu X. Investigating the comprehensive index of acoustic emissions and fractal characteristics of damage of red sandstone based on information entropy. J Nondestruct Eval 2024;43(2):36.
[67] Hosseini S, Azadi M, Ghasemi-Ghalebahman A, Jafari S. Fatigue crack initiation detection in ductile cast iron crankshaft under rotating bending fatigue test using the acoustic emission entropy method. Eng Fail Anal 2023;144:106981.
[68] D'Angela D, Ercolino M. Acoustic emission entropy: an innovative approach for structural health monitoring of fracture-critical metallic components subjected to fatigue loading. Fatigue Fract Eng M 2021;44(4):1041–58.
[69] Shannon C. A mathematical theory of communication. Bell Syst Tech J 1948;27(3):379–423.
[70] Santo F, Sattar T, Edwards G. Validation of acoustic emission waveform entropy as a damage identification feature. Appl Sci 2019;9(19):4070.
[71] Kahirdeh A. Energy dissipation and entropy generation during the fatigue degradation: Application to health monitoring of composites. Louisiana State University and Agricultural & Mechanical College; 2014.
[72] Contoyiannis Y, Potirakis S, Eftaxias K. The earth as a living planet: human-type diseases in the earthquake preparation process. Nat Hazards Earth Syst Sci 2013;13:125–39.
[73] Contoyiannis Y, Kosmidis E, Diakonos F, Kampitakis M, Potirakis S. A hybrid artificial neural network for the generation of critical fluctuations and inter-spike intervals. Chaos Solit Fractals 2022;159:112115.
[74] Friedrich L, Cezar E, Colpo A, Tanzi B, Lacidogna G, Iturrioz I. Identifying impending failure in heterogeneous materials: a study on acoustic emission time series. Chaos Soliton Fract 2024;185:115172.
[75] JCMS-III, B5706. Monitoring method for active cracks in concrete by acoustic emission. JAPAN: Federation of Construction Materials Industries; 2003.
[76] RECOMMENDATION OF RILEM TC 212-ACD. Acoustic emission and related NDE techniques for crack detection and damage evaluation in concrete: Test method for classification of active cracks in concrete by acoustic emission. Mater Struct 2010;43(9):1187–9.
[77] Ohtsu M, Isoda T, Tomoda Y. Acoustic emission techniques standardized for concrete structures. J Acoust Emiss 2007;25:21–32.
[78] Karimian S, Modarres M, Bruck H. A new method for detecting fatigue crack initiation in aluminum alloy using acoustic emission waveform information entropy. Eng Fract Mech 2020;223:106771.
[79] Santo F, Sattar T, Edwards G. Validation of acoustic emission waveform entropy as a damage identification feature. Appl Sci 2019;9(19):4070.
[80] Shateri M, Ghaib M, Svecova D, Thomson D. Acoustic emission signal entropy as a means to estimate loads in fiber reinforced polymer rods. Sensors 2021;21(4):1089.